RSC Advances

PAPER

View Article Online
View Journal | View Issue

Cite this: *RSC Adv.*, 2022, **12**, 12544

$NiCo_2O_4$ thin film prepared by electrochemical deposition as a hole-transport layer for efficient inverted perovskite solar cells†

Sen Wang,[a] Linqin Wang,[b] Chang Liu,[a] Yu Shan,[a] Fusheng Li *[a] and Licheng Sun[ab]

Received 21st March 2022
Accepted 20th April 2022

DOI: 10.1039/d2ra01816k

rsc.li/rsc-advances

Spinel $NiCo_2O_4$ is a promising p-type semiconductor for optoelectronic devices; however, it is difficult to prepare uniform and large-area $NiCo_2O_4$ films, which hinders its application as a hole transport material for perovskite solar cells (PSCs). In this study, a novel, mild, and low-cost KCl-assisted electrochemical deposition (ECD) approach was developed to directly prepare a uniform $NiCo_2O_4$ film on a fluorine-doped tin oxide (FTO) substrate. A uniform $NiCo_2O_4$ film prepared through an ECD approach was used as a hole-transport layer (HTL) in inverted PSCs. The resulting $NiCo_2O_4$ HTL-based device achieved a power conversion efficiency (PCE) of 19.24% with negligible hysteresis and excellent reproducibility. Additionally, it outperformed a NiO_x-based device (PCE = 18.68%). The unsealed devices retained 90.7% of their initial efficiency when subjected to stability measurements for 360 h in an ambient atmosphere. This study shows the great potential of ECD-prepared $NiCo_2O_4$ HTLs for large-area PSCs in the future.

Introduction

Recently, organic-inorganic hybrid perovskite solar cells (PSCs) have attracted tremendous attention owing to their low cost and high power conversion efficiency (PCE).[1–4] In a typical PSC structure, carrier-transport layers (CTLs) connected with perovskite materials could not only improve the charge transfer from the perovskite light absorption layer to the current-collecting electrode, but also block the injection of the opposite charge carrier.[5,6] Meanwhile, the CTL can also act as a protective layer to prevent perovskite from exposure to water and oxygen. Therefore, a suitable CTL is crucial to improve the PCE and stability of PSCs.[7]

Numerous materials have been used as hole-transport layers (HTLs) for PSCs. However, most of the popular hole-transport materials (HTMs) used in conventional n-i-p type PSCs, such as 2,2,7,7-tetrakis(*N*,*N*-di-*p*-methoxyphenyl-amino)-9,9-spirobifluorene (spiro-OMeTAD), polytriarylamine (PTAA), and other molecules, are poor conductors which require extra chemical doping to offset their insufficient mobility and conductivity.[8,9] This decreases the stability and increases costs, thereby hindering the commercial application of these materials as HTLs in PSCs. In inverted-structured PSCs, poly(3,4-ethylenedioxythiophene):poly(styrenesulfonate) (PEDOT:PSS) is frequently employed as an organic HTL. PEDOT:PSS demonstrates excellent electrical conductivity and moderate processing, but its acidic, hydrophilic nature induces the degradation of the perovskite component and sequentially restricts its development as a superior HTL in solar cells.[10] Generally, inorganic HTMs are low-cost and exhibit better physical and chemical stability than that of organic materials. Besides, they also have tunable optical and electrical properties, which made them promising HTLs.[11] Among them, NiO_x materials are one of the most commonly used inorganic HTMs in inverted PSCs. However, they have relatively low intrinsic conductivity, which needs to be addressed prior to their application.[12–14] Ternary oxides are ideal replacements for NiO_x because of their respectable hole extraction and transporting abilities, good conductivity, and tunable optical properties. Early in 2016, Liao and Wang *et al.* reported a $CuAlO_2$ material prepared by magnetron sputtering method, which was employed as hole selective buffer layer in inverted planer PSCs and achieved a PCE of 14.5%.[15] Later, solution-processed $CuGaO_2$ nanoplates were synthesized by a microwave-assisted hydrothermal method by Jen and Chen *et al.*, and the $CuGaO_2$ nanoplates were used as HTL in the n-i-p configuration PSCs with a promising PCE of 18.5% and improved ambient stability.[16] Furthermore, a $Cu_yCr_zO_2$ HTL synthesized by the sol–gel method was reported by Fang and Li *et al.*, and the resulting PSCs achieved a high PCE of 17.19% on glass and 15.53% on flexible PET substrates, which were much higher than mono-metal oxide-based devices.[17]

[a]State Key Laboratory of Fine Chemicals, Institute of Artificial Photosynthesis, DUT-KTH Joint Education and Research Centre on Molecular Devices, Dalian University of Technology, Dalian, 116024, P. R. China. E-mail: fusheng@dlut.edu.cn
[b]Center of Artificial Photosynthesis for Solar Fuels, School of Science, Westlake University, 310024, Hangzhou, China

† Electronic supplementary information (ESI) available. See https://doi.org/10.1039/d2ra01816k

$NiCo_2O_4$ is a p-type semiconductor with a cubic spinel structure, in which Ni ions occupy the octahedral sites while Co ions are distributed across both octahedral and tetrahedral sites.[18] $NiCo_2O_4$ has the advantages of being abundant, relatively inexpensive, and environmentally friendly, making it a promising candidate for future commercialization. These properties are desirable for the use of $NiCo_2O_4$ in various electronic devices, such as supercapacitors,[18] lithium-ion batteries,[19] electrocatalysts for water splitting,[20] *etc*. Besides, $NiCo_2O_4$ has the highest conductivity (500 S cm^{-1}) among transparent conducting oxides, which is much higher compared to a NiO_x-based HTL.[21,22] Additionally, $NiCo_2O_4$ possesses a wide optical bandgap and a deep valence band position, which matches well with the valence band (VB) of perovskite material, especially for $CH_3NH_3PbI_3$ ($MAPbI_3$).[23]

In 2018, Choy *et al.* synthesized well-dispersed $NiCo_2O_4$ nanoparticles (NPs) through a controllable Co–NH_3 deamination reaction in a sol system containing $Ni(OH)_2$ and the resulting inverted-structured PSC based on this $NiCo_2O_4$ HTL yielded a PCE of 18.23% and exhibited high stability.[24] Same year, Choulis *et al.* applied combustion-synthesized ultrasmall $NiCo_2O_4$ NPs as HTL to form inverted-structure PSCs and achieved a PCE of 15.5%.[25] Recently, Jung *et al.* reported the conventional-structured PSCs fabricated with featured HTLs comprising sol–gel-driven $NiCo_2O_4$ and yielded PCEs of up to 18.16%.[23] Akhter *et al.* used $NiCo_2O_4$ NPs synthesized *via* a chemical co-precipitation method as HTLs in n-i-p type PSCs and achieved a PCE of >14%.[26] These work not only demonstrated that ternary oxide $NiCo_2O_4$ could be used as an HTL in PSCs, but also suggested a possible way to synthesize ultrasmall NPs even though the preparation methods for ultrafine $NiCo_2O_4$ NPs are energetically demanding, expensive, and time-consuming. Meanwhile, the above researches show that the spin-coating process is the most commonly adopted strategy for fabricating $NiCo_2O_4$ HTLs, but this method can be relatively inefficient regarding the reduction in the waste of materials. Therefore, an easy, low-cost, and controllable method for preparing compact and uniform $NiCo_2O_4$ HTLs is urgently needed.

As a mature and completely commercialized technology, electrochemical deposition (ECD) is often utilized to prepare nanomaterials on different conductive substrates. Owing to its low cost, low-temperature requirements, large-area production, and precise control, it can be controlled by regulating the deposition time, current, and/or voltage.[27–31] To ensure a good conductivity of the precursor solution, potassium chloride (KCl) is commonly introduced as a supporting electrolyte.[32] In addition, because of the strong adsorption behavior of Cl^-,[33,34] KCl may play an additional role in the nanomaterials formation process *via* ECD technique. In this study, $NiCo_2O_4$ films were prepared *via* a KCl-assisted ECD process to construct HTLs for the first time for $MAPbI_3$-based inverted-structure PSCs (Scheme 1). The aim of this study was to explore the potential of ECD-prepared $NiCo_2O_4$ HTLs for PSCs, and to provide a new perspective on the preparation of advanced HTLs for further enhancement of the PCEs of PSCs *via* ECD methods.

Experimental

Synthesis of $NiCo_2O_4$ and NiO_x films

Patterned fluorine-doped tin oxide (FTO)/glass substrates were successively cleaned in a detergent solution, deionized water, acetone, and isopropanol for 30 min with ultrasonic treatment, respectively. Before using, all substrates were treated with ultraviolet ozone for 20 min. The ECD processes for $NiCo_2O_4$ or NiO_x were carried out with a three-electrode system, where the cleaned FTO glass functioned as the working electrode, a Pt foil was used as the counter electrode, and the reference electrode comprised saturated Ag/AgCl. Three kinds of electrolytes containing 20 mM $Co(NO_3)_2 \cdot 6H_2O$, 10 mM $Ni(NO_3)_2 \cdot 6H_2O$ and different concentrations of KCl (0, 50, and 100 mM) were used, thus the stoichiometric Ni : Co : K ratios for these different electrolytes were 1 : 2 : 0, 1 : 2 : 5, and 1 : 2 : 10, respectively. After the $NiCo_2O_4$ precursors were deposited on the surface of each FTO glass substrate, the films were annealed in a furnace at 300 °C for 2 h in air. The resulting samples are denoted herein as $NiCo_2O_4$ (0-$NiCo_2O_4$, 5-$NiCo_2O_4$, and 10-$NiCo_2O_4$, respectively). For comparison, 30 mM $Ni(NO_3)_2$ in water was selected as the deposition solution for the preparation of NiO_x. The ECD process was carried out by a chronopotentiometry method with a current density of 0.3 mA cm^{-2}. The as-deposited film was then rinsed with deionized water before being annealed in a tube furnace at 300 °C for 1 h.

Device fabrication

PbI_2 (461 mg) and CH_3NH_3I (MAI, 159 mg) were first dissolved in anhydrous dimethylformamide (DMF, 634 μL) and anhydrous dimethyl sulfoxide (DMSO, 70.9 μL), respectively. Then, 3 mol% urea (*versus* PbI_2 or MAI) was added to the solution, and the mixture was then magnetically stirred for 3 h at room temperature in a nitrogen-filled glovebox. The $NiCo_2O_4$ and NiO_x films were then transported to the glovebox for the preparation of perovskite films, which was conducted through a one-step antisolvent-assisted procedure.[35] The precursor solution was spin-coated onto NiO_x or $NiCo_2O_4$ coated FTO at 1000 rpm for 10 s, and 4000 rpm for 30 s in sequence. Then, 200 μL diethyl ether was quickly dripped onto the film at the high-speed step. The resulting film was heated at 65 °C for 1 min, and then at 100 °C for 10 min. Subsequently, a layer of [6,6]-phenyl-C61-butyric acid methyl ester ($PC_{61}BM$; 20 mg mL^{-1} in chlorobenzene) was spin-coated onto the perovskite layer at 1500 rpm for 30 s, following which a thin layer of bathocuproine (BCP; 0.5 mg mL^{-1} in isopropanol) was deposited on top of the $PC_{61}BM$ layer at 5000 rpm for 30 s. Finally, Ag film with 100 nm thickness was thermally evaporated under vacuum (<5×10^{-4} Pa) to form the contact electrode.

Characterizations

The *J–V* curves of the prepared devices were measured under standard 1 sun, AM 1.5 G conditions, with a solar simulator (Newport 94023A, USA), with 0.1 V s^{-1}. The electrochemical impedance spectroscopy (EIS) was performed in the dark at

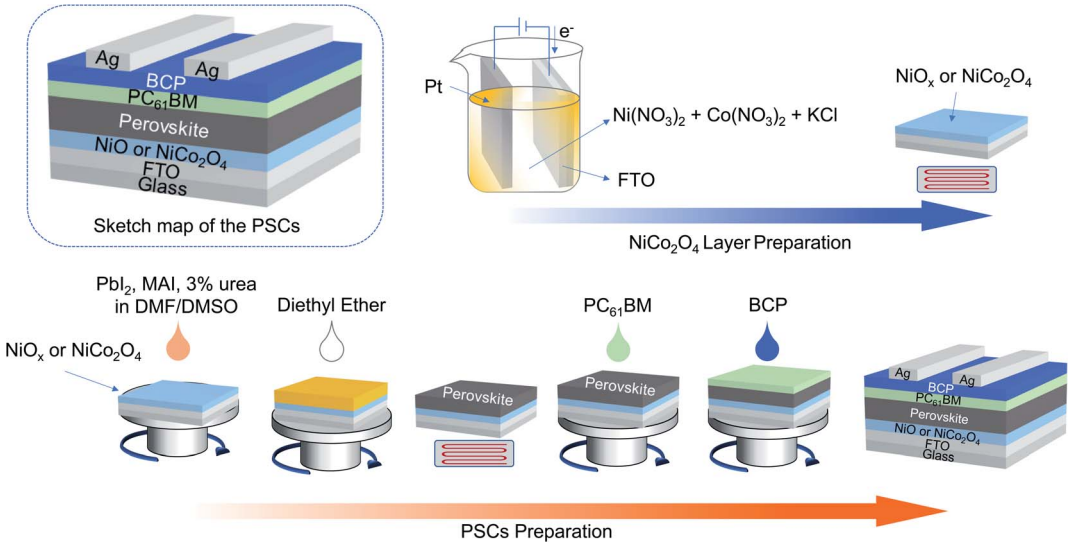

Scheme 1 Schematic illustrations of $NiCo_2O_4$ film fabrication process, prepared *via* electrochemical deposition, and of perovskite solar cell (PSC) preparation procedure. FTO: fluorine-doped tin oxide, DMF: dimethylformamide, DMSO: dimethyl sulfoxide.

a potential of 1.0 V, the frequency was swept from 0.1 Hz to 1 MHz using an electrochemical workstation (Zennium X, Zahner), and the oscillation potential amplitude was adjusted to 10 mV. The crystal structure of NiO_x or $NiCo_2O_4$ film was by X-ray diffraction (XRD, 9 kW, SmartLab). The elemental composition and the energy level of $NiCo_2O_4$ film were characterized by X-ray photoelectron spectroscopy (XPS, ESCALAB XI^+, Thermo Fisher Scientific) and ultraviolet photoelectron spectroscopy (UPS) with a monochromatic He–I light source with an incident energy of 21.22 eV. The morphology of samples was examined by scanning electron microscopy (SEM, SU8220, Hitachi). Optical transmission spectroscopy of NiO_x or $NiCo_2O_4$ film were collected by UV-visible spectrophotometer (Agilent 8453). The electrical performance of NiO_x or $NiCo_2O_4$ film was analyzed by a Hall-effect system (8400, Lake Shore).

Results and discussion

As shown in Scheme 1, the $NiCo_2O_4$ precursor was prepared by chronopotentiometry with a current density of 0.3 mA cm^{-2} for a range of different times. In the inverted-structured PSCs, the perovskite layer based on the as-prepared $NiCo_2O_4$ HTLs was constructed by a one-step antisolvent-assisted procedure, in which a spin-coated $PC_{61}BM$ layer was used as the ETL and Ag was used as the counter electrode.

XRD was used to characterize the crystal structures of the $NiCo_2O_4$ series films on each FTO/glass substrate. As shown in Fig. 1a, the diffraction peaks of the FTO/glass substrate could be detected in all of the XRD patterns of the samples, owing to the ultrathin thickness of the electrodeposited films. In addition to the strong base peaks, three weak diffraction peaks located at 18.9°, 31.1°, and 36.6° were observed, which could be assigned as (111), (220), and (311) crystal planes respectively of the standard patterns of the cubic spinel $NiCo_2O_4$ crystalline phase (JCPDF#73-1072). The XRD results demonstrated that well-crystallized $NiCo_2O_4$ films were obtained *via* ECD method with/without KCl additive.

Optical transmission spectra were conducted to characterize the optical properties of prepared NiO_x and $NiCo_2O_4$ films deposited on the FTO/glass substrate. As shown in Fig. 1b, all samples exhibited almost the same transmission properties as the bare FTO/glass substrate, which maintained a high transmittance (>75% across the spectral range of 400–850 nm). The high transparency of the prepared HTLs minimized the optical losses of the photovoltaic devices and exhibited no competition with the light absorption layer perovskite, thereby ensuring considerable photon-generated carriers. In addition, the optical bandgap of the $NiCo_2O_4$ material was estimated to be 1.88 eV

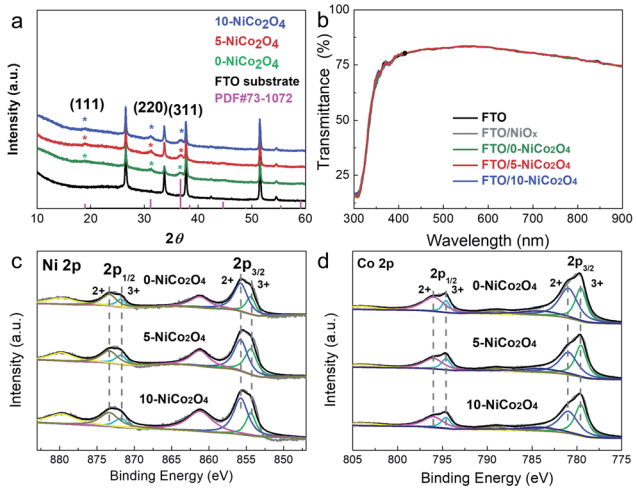

Fig. 1 (a) XRD patterns of $NiCo_2O_4$ films deposited on FTO/glass substrates, (b) optical transmission spectra of NiO_x and different $NiCo_2O_4$ films, and XPS spectra of (c) Ni 2p and (d) Co 2p for the $NiCo_2O_4$ films.

from the Tauc plot (Fig. S1†), which is slightly lower than the previously reported value for $NiCo_2O_4$ NPs.[24]

To further analyze the elemental composition and chemical bonding states of $NiCo_2O_4$ films, XPS measurements were performed. The high-resolution XPS Ni 2p spectrum could be fitted to two spin–orbit doublets and two shakeup satellites (Fig. 1c). The well-fitted peaks at 855.8 eV ($2p_{3/2}$) and 873.4 eV ($2p_{1/2}$) were attributed to the characteristic peaks of the Ni^{2+} oxidation state, and the binding energies of 854.4 eV and 871.8 eV were indexed to Ni^{3+}.[24] According to this, the ratio of Ni^{3+}/Ni^{2+} for 0-$NiCo_2O_4$, 5-$NiCo_2O_4$ and 10-$NiCo_2O_4$ was 0.43, 0.66, and 0.44, respectively, suggesting that optimized KCl additive concentration in deposition precursors was beneficial for the presence of Ni^{3+} state. Additionally, the presence of the Ni^{3+} state could have induced oxygen deficiency in the lattices, and further facilitated the generation of holes in the materials.[23] Besides, the relatively high Ni^{3+}/Ni^{2+} ratios on the surfaces of the $NiCo_2O_4$ films rendered a p-type semiconducting property to the material and increased conductivity, thereby promoting more efficient charge separation and transport.[36,37] For Co 2p, the binding energies of 796.0 eV and 781.0 eV were indexed to Co^{2+}, while the peaks of 794.6 eV and 779.5 eV were associated with Co^{3+} (Fig. 1d). The obtained binding energies of Ni 2p and Co 2p were consistent with previously reported values,[24,38] and no differences were found between the 0-$NiCo_2O_4$, 5-$NiCo_2O_4$, and 10-$NiCo_2O_4$ films.

The morphologies of the NiO_x and $NiCo_2O_4$ films were investigated through SEM characterization. As shown in Fig. 2a, the as-formed NiO_x film had an extremely tiny fluffy porous structure and fully covered the FTO substrate. However, the 0-$NiCo_2O_4$ film had a messy porous structure with numerous intersecting nanosheets (Fig. 2b), resulting in plenty of pinholes and open space sites in the HTL films, which could not ensure complete contact at the HTL/perovskite interface.

Fig. 2c and d illustrate the influence of the KCl additives on the surface morphology of the $NiCo_2O_4$ films. When KCl was added to the deposition solutions, the $NiCo_2O_4$ layers retained their pristine surface morphology covered on the FTO/glass substrates, which is beneficial for the adhesion of perovskite materials on the HTLs. And on this basis, the film quality of the resulting 5-$NiCo_2O_4$ films has been obviously improved, such as larger grain size and better coverage as well as improved compact nanocrystals quality in comparison with NiO_x film (Fig. 2d). These improvements could be mainly attributed to the assistance of KCl in the previous report,[33] which could further promote interface charge extraction and separation.

UPS measurements were performed to investigate the energy levels of the as-prepared $NiCo_2O_4$ films. Relative to the vacuum level, UPS revealed the valence band maximum (VBM) levels to be −4.99 eV, −4.94 eV and −4.79 eV for 0-$NiCo_2O_4$, 5-$NiCo_2O_4$ and 10-$NiCo_2O_4$, respectively (Fig. S2†). The corresponding energy diagram of a PSC based on the prepared $NiCo_2O_4$ HTL is illustrated in Fig. 3a. The VBM levels of samples 0-$NiCo_2O_4$ and 5-$NiCo_2O_4$ were clearly closer to that of $MAPbI_3$ (−5.4 eV), indicating that their energy level matched with that of $MAPbI_3$ very well when acting as HTLs, and would thus ensure efficient hole extraction at the corresponding interfaces. Furthermore, the electrical properties of the NiO_x and $NiCo_2O_4$ layers were evaluated by Hall-effect measurements (Fig. 3b). The electrical conductivity and hole mobility of the $NiCo_2O_4$ films was almost two orders of magnitude higher than those of the NiO_x film, demonstrating the superior charge transport properties of the $NiCo_2O_4$ films. Notably, the 5-$NiCo_2O_4$ film possessed the highest conductivity and hole mobility among all the $NiCo_2O_4$ films. The observed differences in VBM levels and electrical properties of $NiCo_2O_4$ may be attributed to the highest ratio of self-doping created by introducing most Ni^{3+} into the $NiCo_2O_4$ crystal lattice *via* appropriate KCl concentration,[12,39] as discussed in the XPS analysis above.

As shown in Fig. S3,† all of the perovskite films based on the NiO_x and $NiCo_2O_4$ layers exhibited identical crystal structures and similar crystallinities. The main diffraction peaks at 14.16°,

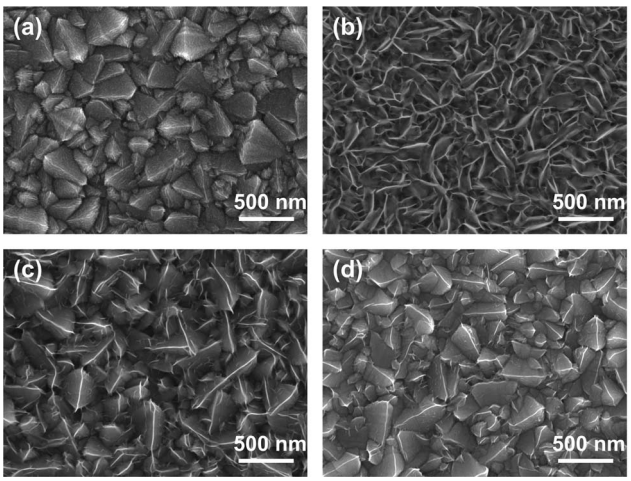

Fig. 2 Top-view SEM images of (a) NiO_x film, and (b) 0-$NiCo_2O_4$, (c) 5-$NiCo_2O_4$, and (d) 10-$NiCo_2O_4$ films deposited on FTO substrates.

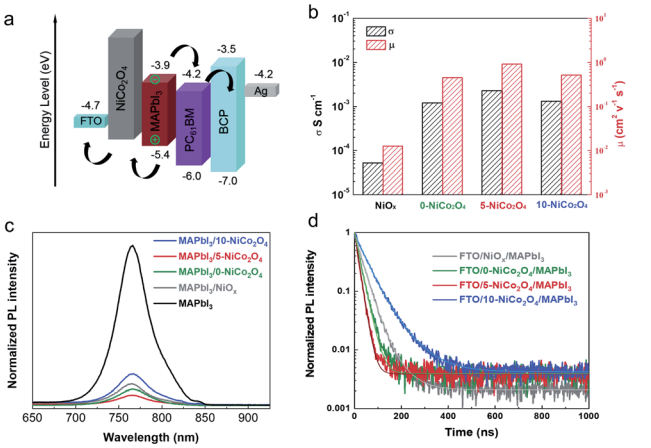

Fig. 3 (a) Energy band diagram relative to a vacuum level of the device. (BCP: bathocuproine) (b) Hall-effect measurements of NiO_x and $NiCo_2O_4$ films. (c) Steady-state photoluminescence of $MAPbI_3$ based on NiO_x and $NiCo_2O_4$ films. (d) Time-resolved photoluminescence spectra of the perovskite films on NiO_x and $NiCo_2O_4$ HTLs.

28.78°, and 31.92° corresponded to the (110), (220), and (310) crystal planes of the perovskite ($MAPbI_3$), respectively. No impurity peaks were observed, except for one weak peak located at 12.6° which was indexed to traces of excess PbI_2. The strongest peak intensity of perovskite/5-$NiCo_2O_4$ suggested the best perovskite crystallinity on the 5-$NiCo_2O_4$ layer, while a similar phenomenon could be convinced by the top-view SEM images as shown in Fig. S4.† Less and smaller cracks appear in the $NiCo_2O_4$ supported perovskite layer. Especially for the perovskite/5-$NiCo_2O_4$ film, smooth and dense film morphologies were displayed with full surface coverage. These comparably high-quality films could directly influence solar cell performance. It can be seen from the UV-vis spectroscopy that the perovskite films based on NiO_x and different $NiCo_2O_4$ HTLs exhibit similar absorption over the entire visible region (Fig. S5†).

The charge transfer dynamics of perovskite films deposited on NiO_x or $NiCo_2O_4$ were studied *via* steady-state photoluminescence (PL) and time-resolved photoluminescence (TRPL) measurements with excitation at 550 nm. As shown in Fig. 3c, the highest PL intensity was observed for the bare $MAPbI_3$ film. After the introduction of the HTLs, the PL intensity decreased drastically, following the order of: $MAPbI_3$/10-$NiCo_2O_4$ > $MAPbI_3/NiO_x$ > $MAPbI_3$/0-$NiCo_2O_4$ > $MAPbI_3$/5-$NiCo_2O_4$. $MAPbI_3$/5-$NiCo_2O_4$ exhibited the highest degree of PL quenching, which means it achieved the best hole extraction and transport efficiency from perovskite to the HTL. This finding agrees well with its suitable energy level alignment and outstanding electrical properties, as discussed above. Fig. 3d shows the TRPL spectra of $MAPbI_3$ films deposited on different HTLs. The PL decay curves have been fitted using a bi-exponential decay function as following eqn (1) and the corresponding parameters are summarized in Table S1.†

$$f(t) = A_1 \exp^{(-t/\tau)} + A_2 \exp^{(-t/\tau)} + B \quad (1)$$

where the fast component τ_1 is ascribed to the charge extraction at the HTL/perovskite interface, while the slow component τ_2 is related to the bimolecular recombination process in bulk perovskite film.[40] A_1 and A_2 represent the contribution proportion of fast and slow component, respectively. Table S1† shows the corresponding parameters of the TRPL spectroscopy. The decrease of fast component τ_1 indicated the faster hole transfer from perovskite to HTL. The high proportion of τ_1 indicated that charge extraction at the HTL/perovskite interface is dominant in the PL quenching process rather than undergoing the bimolecular recombination in bulk perovskite. These results are in good agreement with recently reported results that the bimolecular recombination in perovskite film is negligible at a low light intensity, and it begins to dominate only when the light intensity is around 100 suns.[41] The $MAPbI_3$ film on NiO_x substrate exhibited the average decay time (τ_{ave}) of 42.63 ns for photogenerated excitons, whereas the perovskite films deposited on 0-$NiCo_2O_4$, 5-$NiCo_2O_4$ and 10-$NiCo_2O_4$ HTLs showed the τ_{ave} of 34.34, 31.74 and 64.68 ns, respectively. The rapid decay of PL is evidence of efficient hole extraction at the interface between perovskite and HTL, which is in good agreement with the steady-state PL results.

To probe the effect of $NiCo_2O_4$ film as HTL on device performance, we firstly fabricated the inverted-structure PSCs (FTO/$NiCo_2O_4$/$MAPbI_3$/$PC_{61}BM$/BCP/Ag) with different thicknesses of 0-$NiCo_2O_4$ film (different deposition charge density) by a one-step antisolvent-assisted procedure. Fig. S6a† shows the *J–V* characteristic curves for the respective champion device, and the corresponding device parameters are summarized in Table S2.† Obviously, with the increase of deposition charge density for $NiCo_2O_4$ film, the device performance presented a tendency to increase first and then decrease. The thinner $NiCo_2O_4$ layer-based PSC (5 mC cm^{-2}) displayed a inferior performance with a low current density. This can be attributed to the current leakage resulting from incomplete coverage of $NiCo_2O_4$ on FTO substrate. Meanwhile, the thicker $NiCo_2O_4$ layer-based PSC (20 mC cm^{-2}) was also subjected to a poor current density due to the increase of series resistance (R_s). And the optimum thickness of $NiCo_2O_4$ layer was found to be a charge density of 10 mC cm^{-2}, which resulted in a PCE of 18.66% with J_{sc} of 22.93 mA cm^{-2}, V_{oc} of 1.02 V, and fill factor (FF) of 0.78. The results were further confirmed by the efficiency distributions as a function of deposition charge density, as shown in Fig. S6b.†

We further fabricated the inverted PSCs based on NiO_x and different $NiCo_2O_4$ HTLs at the charge density of 10 mC cm^{-2}, the *J–V* characteristic curves of the respective champion devices are shown in Fig. 4a, and the corresponding photovoltaic parameters are summarized in Table 1. The *J–V* curves of champion devices based on NiO_x and 0-$NiCo_2O_4$ HTLs almost overlapped. Among all the devices, the 5-$NiCo_2O_4$ HTL-based device displayed the highest PCE of 19.24%,

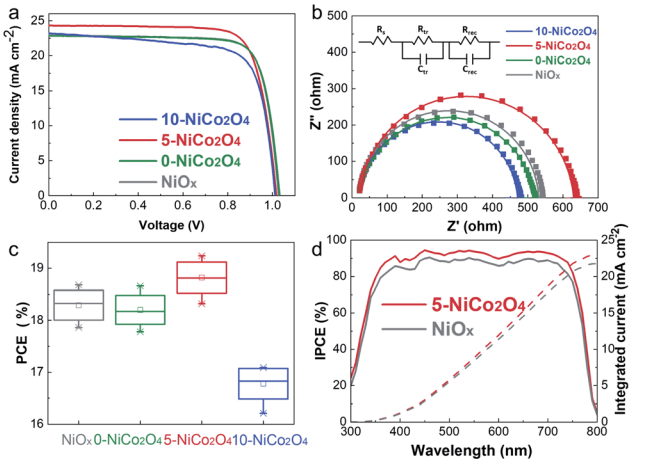

Fig. 4 (a) *J–V* characteristics of best NiO_x and $NiCo_2O_4$-based PSCs measured under illumination (1 sun). (b) Nyquist plots of PSCs based on NiO_x and $NiCo_2O_4$ HTLs for electrochemical impedance spectroscopy (EIS) experiments. Solid lines show fitting curves. (c) Statistics of ten pieces of each PSCs based on NiO_x and $NiCo_2O_4$ HTLs. (d) Incident-photon-to-current efficiencies (IPCEs) of PSCs based on NiO_x and 5-$NiCo_2O_4$ HTLs under monochromatic light with varying wavelengths. Dashed lines represent corresponding integrating currents over AM 1.5 G solar irradiance spectra.

Table 1 Photovoltaic parameters of PSCs based on NiOx and $NiCo_2O_4$ HTLs under the illumination

HTL	V_{oc} (V)	J_{sc} (mA cm^{-2})	FF (%)	PCE (%)
NiO_x	1.03	22.86	79.61	18.69
0-$NiCo_2O_4$	1.03	22.84	79.31	18.66
5-$NiCo_2O_4$	1.02	24.31	77.89	19.24
10-$NiCo_2O_4$	1.01	23.14	73.09	17.09

a short-circuit current density (J_{sc}) of 24.31 mA cm^{-2}, a fill factor (FF) of 0.78, and an open-circuit voltage (V_{oc}) of 1.02 V. The J_{sc} of the 5-$NiCo_2O_4$ HTL-based device improved from 22.83 to 24.31 mA cm^{-2} compared with that of the 0-$NiCo_2O_4$ based device, which can be attributed to the smoothest surface morphology of 5-$NiCo_2O_4$ and complete contact with the perovskite layer, as well as best hole extraction ability, hole mobility and conductivity. The 10-$NiCo_2O_4$ HTL-based device delivered a poor efficiency with a low V_{oc} and FF, owing to its mismatched energy level compared to the perovskite layer. Furthermore, Fig. 4c provides statistical data regarding the reproducibility of the performances of the NiOx- and $NiCo_2O_4$-based PSCs. These results are in good agreement with the statistical efficiency distributions of the different devices. The average PCE for the NiO_x HTL-based devices obtained from the ten devices was 18.17 ± 0.32%; this increased to 18.94 ± 0.29% for 5-$NiCo_2O_4$. The photovoltaic performance disadvantage of $NiCo_2O_4$-based devices is the relatively low open-circuit voltage (V_{oc}), resulting from the nonradiative recombination losses at the HTL/perovskite interface. To address this issue, it is necessary to minimize the energy barrier at the interface. Small organic molecules with high electron affinity, such as F4TCNQ, could shift the Fermi level of HTMs toward the VBM of perovskite, which is a feasible strategy to reduce the interfacial energy barrier and strengthen the p-type property of HTM. This research on boosting the open-circuit voltage will continue to be discussed in future work.

EIS measurements were performed to give a closer inspection of the charge transport process and recombination process at the interfaces.[14] As shown in Fig. 4b, only one semicircle was observed for each sample, which corresponds to the recombination resistance (R_{rec}). The largest semicircle belonged to the 5-$NiCo_2O_4$ HTL-based device, which revealed that the carrier recombination at the interfaces between the HTL and perovskite layer was retarded. The semicircle of the NiO_x device was slightly larger than that of the 0-$NiCo_2O_4$-based device, corresponding to the photovoltaic performances of the two devices (Fig. 4a and Table 1). The lowest R_{rec} was obtained for the 10-$NiCo_2O_4$ based device, which correlated well with the observed decreases in V_{oc} and FF. As discussed above, the 5-$NiCo_2O_4$ HTL-based PSC had the lowest interfacial recombination loss, which was beneficial for faster charge transfer and collection across the device, thus resulting in a higher PEC. Besides, we measured the dark *J–V* curves of PSCs incorporated with NiO_x and different $NiCo_2O_4$ HTLs, as depicted in Fig. S7.† The dark current density decreases in the order of 10-$NiCo_2O_4$> NiO_x> 0-$NiCo_2O_4$ > 5-$NiCo_2O_4$, indicating that 5-$NiCo_2O_4$-based device possesses better diode behavior with lower leakage current density.

As photocurrent hysteresis was a major issue in the accurate characterization of device efficiency, the typical *J–V* curves were measured for PSCs based on the NiO_x and 5-$NiCo_2O_4$ HTLs, with both reverse and forward scan directions (Fig. S8a†). The 5-$NiCo_2O_4$ HTL-based PSCs exhibited slight hysteresis in the *J–V* curves, and the reverse and forward scanning directions yielded PCEs of 19.73 and 19.24%, respectively (a difference of 0.49%, as listed in Table S4†). Meanwhile, the steady-state power output at the maximum power point for the optimized devices was recorded in Fig. S8b,† where the PCE of the 5-$NiCo_2O_4$ HTL-based PSC rose directly to a steady-state, yielding a maximum PCE value of 19.37% at 0.87 V. Low hysteresis and the quick photoelectric response could be attributed to the efficient charge separation and transport promoted by 5-$NiCo_2O_4$, which significantly suppressed interfacial charge recombination between the HTL and perovskite.[16]

The incident-photon-to-current efficiencies (IPCEs) of PSCs based on NiO_x and 5-$NiCo_2O_4$ HTLs were measured (Fig. 4d). As the wavelength was gradually increased from 300 to 800 nm, the IPCE of the PSC based on the 5-$NiCo_2O_4$ HTL remained higher than that of the NiO_x HTL-based PSC. Moreover, photocurrents of 22.98 mA cm^{-2} and 21.78 mA cm^{-2} were obtained by integrating the IPCE curves for PSCs based on 5-$NiCo_2O_4$ and NiO_x HTLs over the AM 1.5 G solar irradiation spectrum. These values are consistent with the experimentally measured J_{sc} values.

The long-term stabilities of unencapsulated PSCs based on the 5-$NiCo_2O_4$ and NiO_x HTLs were investigated in an ambient atmosphere at room temperature with humidity of 30–40% (Fig. 5). As the aging time was extended to approximately 360 h, the PCEs of the device fabricated on the 5-$NiCo_2O_4$ HTL remained at 90.7% of the initial efficiency. As a comparison, the PCE of the device based on NiO_x HTL retained less than 90% of its initial efficiency after only 288 h aging time under the same condition.

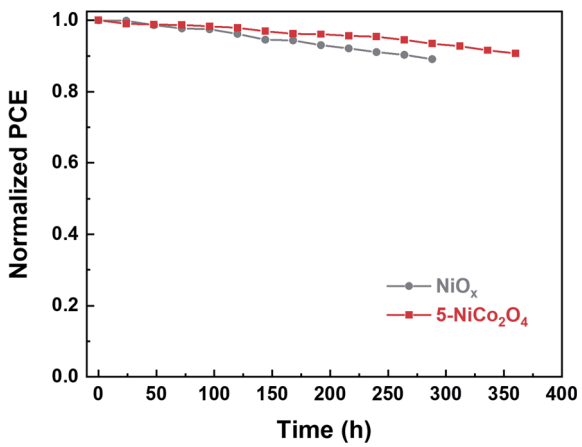

Fig. 5 Long-term stability of the devices based on NiO_x and 5-$NiCo_2O_4$ HTLs stored at ambient conditions with humidity of 30–40%.

Conclusions

For the first time, $NiCo_2O_4$ films obtained by ECD method were employed as HTLs to obtain efficient and stable PSCs. Notably, when a suitable amount of KCl additive was added to the deposition solution, a smooth and compact $NiCo_2O_4$ layer could be obtained, which was beneficial for the contact of the perovskite layer covered on the $NiCo_2O_4$ HTL. Meanwhile, the p-type semiconductor property and electrical conductivity could both be enhanced, leading to efficient charge separation and transport between perovskite and the $NiCo_2O_4$ HTL. Thus, a PCE of 19.24% was obtained for the $NiCo_2O_4$ HTL-based champion device, with negligible hysteresis, excellent reproducibility, and long-term stability. In addition, this PCE was better than that of a NiO_x HTL-based PSC (18.68%). This study shows the huge potential of ECD-prepared $NiCo_2O_4$ HTLs for PSCs, and the findings presented here could provide a novel perspective on the preparation of advanced HTLs for further enhancement of PSCs performance and large-scale application.

Conflicts of interest

There are no conflicts of interest to declare.

Acknowledgements

This work was financially supported by the National Natural Science Foundation of China (NSFC; Grant No. 22172011), and the Key Laboratory of Bio-based Chemicals of Liaoning Province of China. L. Wang thanks Zhejiang Province Selected Funding for Postdoctoral Research Projects (ZJ2021001) for financial support.

Notes and references

1 X. Zheng, Y. Hou, C. Bao, J. Yin, F. Yuan, Z. Huang, K. Song, J. Liu, J. Troughton, N. Gasparini, C. Zhou, Y. Lin, D.-J. Xue, B. Chen, A. K. Johnston, N. Wei, M. N. Hedhili, M. Wei, A. Y. Alsalloum, P. Maity, B. Turedi, C. Yang, D. Baran, T. D. Anthopoulos, Y. Han, Z.-H. Lu, O. F. Mohammed, F. Gao, E. H. Sargent and O. M. Bakr, *Nat. Energy*, 2020, **5**, 131–140.

2 J. Burschka, A. Dualeh, F. Kessler, E. Baranoff, N.-L. Cevey-Ha, C. Yi, M. K. Nazeeruddin and M. Grätzel, *J. Am. Chem. Soc.*, 2011, **133**, 18042–18045.

3 D. Stranks Samuel, E. Eperon Giles, G. Grancini, C. Menelaou, J. P. Alcocer Marcelo, T. Leijtens, M. Herz Laura, A. Petrozza and J. Snaith Henry, *Science*, 2013, **342**, 341–344.

4 Best Research Cell Efficiencies, **https://www.nrel.gov/pv/assets/pdfs/best-research-cell-efficiencies-rev211117.pdf**.

5 V. Gonzalez-Pedro, E. J. Juarez-Perez, W.-S. Arsyad, E. M. Barea, F. Fabregat-Santiago, I. Mora-Sero and J. Bisquert, *Nano Lett.*, 2014, **14**, 888–893.

6 T. Wu, Z. Qin, Y. Wang, Y. Wu, W. Chen, S. Zhang, M. Cai, S. Dai, J. Zhang, J. Liu, Z. Zhou, X. Liu, H. Segawa, H. Tan, Q. Tang, J. Fang, Y. Li, L. Ding, Z. Ning, Y. Qi, Y. Zhang and L. Han, *Nano-Micro Lett.*, 2021, **13**, 152.

7 J. Yan, T. J. Savenije, L. Mazzarella and O. Isabella, *Sustainable Energy Fuels*, 2022, **6**, 243–266.

8 J. H. Noh, N. J. Jeon, Y. C. Choi, M. K. Nazeeruddin, M. Grätzel and S. I. Seok, *J. Mater. Chem. A*, 2013, **1**, 11842–11847.

9 P. Mahajan, B. Padha, S. Verma, V. Gupta, R. Datt, W. C. Tsoi, S. Satapathi and S. Arya, *J. Energy Chem.*, 2022, **68**, 330–386.

10 J. R. Manders, S.-W. Tsang, M. J. Hartel, T.-H. Lai, S. Chen, C. M. Amb, J. R. Reynolds and F. So, *Adv. Funct. Mater.*, 2013, **23**, 2993–3001.

11 H. Zhang, H. Wang, H. Zhu, C.-C. Chueh, W. Chen, S. Yang and A. K. Y. Jen, *Adv. Energy Mater.*, 2018, **8**, 1702762.

12 W. Chen, Y. Wu, Y. Yue, J. Liu, W. Zhang, X. Yang, H. Chen, E. Bi, I. Ashraful, M. Grätzel and L. Han, *Science*, 2015, **350**, 944–948.

13 W. Chen, F.-Z. Liu, X.-Y. Feng, A. B. Djurišić, W. K. Chan and Z.-B. He, *Adv. Energy Mater.*, 2017, **7**, 1700722.

14 T. Wang, D. Ding, H. Zheng, X. Wang, J. Wang, H. Liu and W. Shen, *Sol. RRL*, 2019, **3**, 1900045.

15 F. Igbari, M. Li, Y. Hu, Z.-K. Wang and L.-S. Liao, *J. Mater. Chem. A*, 2016, **4**, 1326–1335.

16 H. Zhang, H. Wang, W. Chen and A. K. Y. Jen, *Adv. Mater.*, 2017, **29**, 1604984.

17 P.-L. Qin, Q. He, C. Chen, X.-L. Zheng, G. Yang, H. Tao, L.-B. Xiong, L. Xiong, G. Li and G.-J. Fang, *Sol. RRL*, 2017, **1**, 1700058.

18 Z. Wu, Y. Zhu and X. Ji, *J. Mater. Chem. A*, 2014, **2**, 14759–14772.

19 Y. Li, X. Wu, S. Wang, W. Wang, Y. Xiang, C. Dai, Z. Liu, Z. He and X. Wu, *RSC Adv.*, 2017, **7**, 36909–36916.

20 C. Zhu, S. Fu, D. Du and Y. Lin, *Chem. - Eur. J.*, 2016, **22**, 4000–4007.

21 R. R. Owings, G. J. Exarhos, C. F. Windisch, P. H. Holloway and J. G. Wen, *Thin Solid Films*, 2005, **483**, 175–184.

22 F. Yang, X. Tian, Y. Gu, K. Zhang and L. Liu, *RSC Adv.*, 2019, **9**, 24880–24887.

23 J. H. Lee, Y. W. Noh, I. S. Jin, S. H. Park and J. W. Jung, *J. Mater. Chem. C*, 2019, **7**, 7288–7298.

24 D. Ouyang, J. Xiao, F. Ye, Z. Huang, H. Zhang, L. Zhu, J. Cheng and W. C. H. Choy, *Adv. Energy Mater.*, 2018, **8**, 1702722.

25 I. T. Papadas, A. Ioakeimidis, G. S. Armatas and S. A. Choulis, *Adv. Sci.*, 2018, **5**, 1701029.

26 A. Bashir, S. Shukla, R. Bashir, R. Patidar, A. Bruno, D. Gupta, M. S. Satti and Z. Akhter, *Sol. Energy*, 2020, **196**, 367–378.

27 F. Li, Y. Li, Q. Zhuo, D. Zhou, Y. Zhao, Z. Zhao, X. Wu, Y. Shan and L. Sun, *ACS Appl. Mater. Interfaces*, 2020, **12**, 11479–11488.

28 Z. Zhao, S. Zhan, L. Feng, C. Liu, M. S. G. Ahlquist, X. Wu, K. Fan, F. Li and L. Sun, *ACS Appl. Mater. Interfaces*, 2021, **13**, 40602–40611.

29 T. Wang, D. Ding, X. Wang, R. Zeng, H. Liu and W. Shen, *ACS Omega*, 2018, **3**, 18434–18443.

30 I. J. Park, G. Kang, M. A. Park, J. S. Kim, S. W. Seo, D. H. Kim, K. Zhu, T. Park and J. Y. Kim, *ChemSusChem*, 2017, **10**, 2660–2667.
31 X. Miao, S. Wang, W. Sun, Y. Zhu, C. Du, R. Ma and C. Wang, *Scr. Mater.*, 2019, **165**, 134–139.
32 R. Tena-Zaera, J. Elias, G. Wang and C. Lévy-Clément, *J. Phys. Chem. C*, 2007, **111**, 16706–16711.
33 R. Tena-Zaera, J. Elias, C. Lévy-Clément, C. Bekeny, T. Voss, I. Mora-Seró and J. Bisquert, *J. Phys. Chem. C*, 2008, **112**, 16318–16323.
34 Y. Mastai, D. Gal and G. Hodes, *J. Electrochem. Soc.*, 2000, **147**, 1435.
35 X. Zhang, H. Xiong, J. Qi, C. Hou, Y. Li, Q. Zhang and H. Wang, *ACS Appl. Energy Mater.*, 2018, **1**, 6477–6486.
36 I. Sullivan, B. Zoellner and P. A. Maggard, *Chem. Mater.*, 2016, **28**, 5999–6016.
37 A. Barnabé, Y. Thimont, M. Lalanne, L. Presmanes and P. Tailhades, *J. Mater. Chem. C*, 2015, **3**, 6012–6024.
38 Y. Zhang, B. Wang, F. Liu, J. Cheng, X.-w. Zhang and L. Zhang, *Nano Energy*, 2016, **27**, 627–637.
39 J. H. Kim, P.-W. Liang, S. T. Williams, N. Cho, C.-C. Chueh, M. S. Glaz, D. S. Ginger and A. K. Y. Jen, *Adv. Mater.*, 2015, **27**, 695–701.
40 P. Zhu, S. Gu, X. Luo, Y. Gao, S. Li, J. Zhu and H. Tan, *Adv. Energy Mater.*, 2020, **10**, 1903083.
41 Y. Chen, Z. Yang, S. Wang, X. Zheng, Y. Wu, N. Yuan, W.-H. Zhang and S. Liu, *Adv. Mater.*, 2018, **30**, 1805660.